Remote sensing of three-dimensional cirrus clouds from satellites: application to continuous-wave laser atmospheric transmission and backscattering

K. N. Liou, Szu-Cheng Ou, Yoshihide Takano, and Jeffrey Cetola

A satellite remote sensing methodology has been developed to retrieve 3D ice water content (IWC) and mean effective ice crystal size of cirrus clouds from satellite data on the basis of a combination of the conventional retrieval of cloud optical depth and particle size in a horizontal plane and a parameterization of the vertical cloud profile involving temperature from sounding and/or analysis. The inferred 3D cloud fields of IWC and mean effective ice crystal size associated with two impressive cirrus clouds that occurred in the vicinity of northern Oklahoma on 18 April 1997 and 9 March 2000, obtained from the Department of Energy's Atmospheric Radiation Measurement Program, have been validated against the ice crystal size distributions that were collected independently from collocated and coincident aircraft optical probe measurements. The 3D cloud results determined from satellite data have been applied to the simulation of cw laser energy propagation, and we show the significance of 3D cloud geometry and inhomogeneity and spherical atmosphere on the transmitted and backscattered laser powers. Finally, we demonstrate that the 3D cloud fields derived from satellite remote sensing can be used for the 3D laser transmission and backscattering model for tactical application.   © 2006 Optical Society of America

OCIS codes: 280.0280, 120.0280, 140.0140, 010.3310.

1. Introduction

The time series of backscattering coefficients derived from the ground-based lidar and cloud radar returns[1–3] have shown significant vertical variability in ice water content (IWC) and ice crystal size. Vertical inhomogeneity of the ice crystal size and IWC has also been observed in the balloonborne replicator sounding observations.[4] The vertical inhomogeneity of ice crystal size can alter the radiative heating profile in cirrus clouds and hence is an important component in the radiation–climate feedback study.[5] It can also affect the propagation of active radiation sources in cloud layers. However, the present satellite remote sensing technique can only retrieve vertically integrated optical and microphysical properties of cirrus clouds.[6–12] Cirrus clouds are high clouds that are present at all latitudes and in all seasons with a global average of approximately 20%–30% and more than 60%–70% in the tropics.[13] Some of these high cirrus clouds are optically thin with optical depths less than 0.5 (Refs. 14 and 15) and often subvisual. In this paper, we have developed a parameterization approach to derive 3D cloud IWC and ice crystal size distributions based on satellite data and provided a number of independent validations employing concurrent and simultaneous *in situ* ice microphysics measurements from the aircraft platform under the satellite passage.

In conjunction with high-energy laser propagation in the atmosphere, we have presented 1D and 2D laser transmission models in plane-parallel and spherical geometries associated with the aircraft–cirrus–target system.[16–18] Using the successive order-of-scattering approach for radiative transfer, direct and diffuse transmissions were formulated specifically for homogeneous high-level clouds, in which scattering and absorption associated with aerosols, water vapor, and air molecules were accounted for. In the 2D laser transmission model,[18] it was assumed that cloud properties only vary in the vertical plane (x–z plane), thus neglecting the variation of the cloud properties in the y direction. Moreover, the 3D nature of the laser beam has not been accounted for in the 2D formulation. To accurately simulate the 3D laser transmission–

K. N. Liou, S.-C. Ou (ssou@atmos.ucla.edu), and Y. Takano are with the Department of Atmospheric and Oceanic Sciences, University of California, Los Angeles, Los Angeles, California 90095-1565. J. Cetola is with the Airborne Laser Program System Office, Kirtland Air Force Base, New Mexico 87117-6612.

backscattering in high-level cloud fields, a 3D approach must be taken. In association with the mapping of 3D cloud fields from satellite remote sensing, we formulated and developed a 3D laser transmission–backscattering model, taking into account the Earth's spherical geometry and the 3D finite and inhomogeneous structure of high-level cloud fields to investigate the significance of the 3D nature of clouds on laser energy propagation in the atmosphere.

This paper is organized as follows: Section 2 presents a parameterization approach to the mapping of 3D inhomogeneous cirrus cloud fields from satellite data and application of the 3D cirrus cloud remote sensing method to Atmospheric Radiation Measurement (ARM) Cloud Intensive Operational Period (IOP) data with an independent validation of its accuracy by using *in situ* aircraft microphysical measurements. A description of the basic formulation and analysis of 3D laser transmission and backscattering through cirrus clouds follows in Section 3, including an assessment of the importance of 3D cloud effects on high-energy laser transmission. Finally, concluding remarks are given in Section 4.

2. Satellite Mapping of Three-Dimensional Inhomogeneous Cirrus Clouds

A. Parameterization Approach
A number of approaches have been developed for the inference of the horizontal distributions of cirrus cloud optical depth and ice crystal size from satellites. These approaches used wavelengths at which absorption by water vapor and other gases is minimal and at which scattering and absorption by cloud particles exhibit maximum sensitivity. Reflectance correlation of a nonabsorbing wavelength (e.g., a visible wavelength) and an absorbing wavelength (e.g., wavelengths at 1.6, 2.2, or 3.7 μm) has been established by radiative transfer calculations *a priori* in terms of lookup tables for the simultaneous retrieval of optical depth and ice crystal size.[7–10] The cloud optical depth by definition refers to the vertically integrated value, while the particle size retrieved is related to its mean property in the vertical. Thus, the present satellite retrieval techniques are limited to the horizontal mapping of the cloud optical and microphysical properties. By combining the horizontal mapping of cloud parameters from satellites with the retrieval of the vertical distributions of IWC and ice crystal size parameters from the reflectivity and Doppler velocity of a millimeter-wave cloud radar (mmCR), Liou *et al.*[19] showed that 3D distributions of IWC and ice crystal mean size can be inferred. This novel approach, however, is restricted to single points where cloud radar observations are available. In the following, we develop a parameterization approach to determine the regional 3D cloud structure entirely from satellite data with a global perspective. We will also present limited validations of the present approach based on available cloud microphysics measurements. Our approach focuses on global application and the use of satellite data and is not intended to account for local small-scale cloud variability that can be simulated from stochastic cloud models.[20,21]

We first let the horizontal distribution of the optical depth and mean effective ice crystal size retrieved from satellite data be denoted by $\tau(x, y)$ and DE*(x, y), respectively. We define DE in the form

$$\text{DE} = \int D^2 Ln(L)\text{d}L \bigg/ \int DLn(L)\text{d}L, \qquad (2.1)$$

where D and L denote the width and the maximum dimension of a nonspherical ice crystal, respectively, and $n(L)$ is the size distribution in terms of L. The preceding definition of the mean effective size is closely related to the ratio of the total ice crystal volume to the total ice crystal cross-sectional area and is applicable to irregular and complex ice crystal shapes. Based on cloud microphysics observations and radiative transfer parameterizations, ice crystal size can be defined in terms of cloud temperature, IWC, and optical depth.[22–26] Moreover, ice crystal size is approximately proportional to the 1/3 power of IWC.[22] Thus, on the basis of dimensional analysis, we have developed the following parameterization for the 3D distribution of DE in the form[22]

$$\begin{aligned}\text{DE}(x, y, z) = c\{\tau(x, y)/[\Delta z(\alpha + \beta/\langle\text{DE}(z)\rangle) \\ \times \langle\text{IWC}(z)\rangle]\}^{1/3}\langle\text{DE}(z)\rangle,\end{aligned} \qquad (2.2)$$

where τ is the visible optical depth, c is a proportional factor, Δz is the cloud thickness, α and β are empirical constants, and the terms

$$\langle\text{DE}(z)\rangle = \sum_{n=0}^{3} c_n(T_c(z) - 273)^n, \qquad (2.3)$$

$$\begin{aligned}\langle\text{IWC}(z)\rangle = \exp\big(-7.6 + 4\exp\{-0.2443 \times 10^{-3} \\ \times [253 - T_c(z)]\}^{2.445}\big) \\ \text{for } T_c(z) < 253 \text{ K.}\end{aligned} \qquad (2.4)$$

In Eqs. (2.3) and (2.4), the local values of DE and IWC denoted by $\langle\cdot\rangle$ are related to the local cloud temperature T_c. Information about T_c (as a function of height) can be obtained via local sounding. Temperature data may also be obtained from the conventional retrieval using vertical sounding channels[27] or from the National Centers for Environmental Prediction (NCEP) global analysis product.[28]

The proportionality factor c can be determined by performing a vertical averaging of Eq. (2.2), and equating the resulting vertical mean $\overline{\text{DE}}(x, y)$ with the satellite-retrieved mean effective size, DE*(x, y), as follows:

$$\begin{aligned}c = \text{DE}^*(x, y)\big(\tau(x, y)/\{\Delta z[\alpha + \beta/\text{DE}^*(x, y)] \\ \times \langle\text{IWC}\rangle\}\big)^{-1/3}\langle\overline{\text{DE}}\rangle^{-1}.\end{aligned} \qquad (2.5)$$

Finally, the 3D IWC can now be expressed via a radiative transfer parameterization by[29]

$$IWC(x, y, z) = \tau(x, y) / \{\Delta z[\alpha + \beta / DE(x, y, z)]\}. \tag{2.6}$$

The methodology for the remote sensing of 3D cloud fields outlined above is based on a number of physical approximations and local microphysics observations and does not require the use of ground-based lidar–radar data. Obviously, its success requires independent validation. We present two case studies to illustrate the fundamental principle and numerical procedure of the present approach. For these two cases, collocated and coincident cirrus cloud microphysical data available from *in situ* aircraft measurements during the same time period of the satellite passage were used for an independent check of the retrieval results. It should be noted that collocated and coincident satellite and *in situ* aircraft data requires a carefully planned field campaign and its availability is extremely limited.

B. Validation Using Department of Energy–Atmospheric Radiation Measurement Data

To cross-check the validity of the parameterization approach for the mapping of 3D cloud fields based on satellite data, we have selected Advanced Very High-Resolution Radiometer–National Oceanic and Atmospheric Administration (AVHRR–NOAA) data gathered at the ARM Southern Great Plains (SPG) Cloud and Radiation Testbed (CART) site in the northern Oklahoma area for single-layer cirrus clouds that occurred on 18 April 1997 and 9 March 2000 during two Spring Cloud IOPs. Retrieval and analysis were carried out to construct 3D IWC and DE fields from the AVHRR data, which were then compared to collocated and coincident *in situ* measurements of the ice crystal size distribution and IWC independently derived from the optical probes onboard the University of North Dakota Citation.

During the ARM Spring Cloud IOP at the SGP on 1–26 March 2000, there was a significant stratiform cirrus cloud episode occurring on 9 March. Well-defined cirrus clouds started to appear over the Central Facility site after 1500 UTC, reaching peak activity around 2100 UTC, before breaking up. Although NASA/Terra was launched three months before this date, Moderate Resolution Imaging Spectroradiometer (MODIS) data for this date was not available owing to insufficient calibration accuracy. However, NOAA-14 passed over the SGP site at 2206 UTC with a good viewing angle and AVHRR data was available for 3D cloud studies. The horizontal mapping of cloud parameters is based on the correlation approach for the 0.63 μm reflectance and the 3.7 μm total radiance as functions of reference optical depth and DE constructed from plane-parallel radiative transfer calculations in terms of lookup tables by prescribing the single-scattering properties for ice particles *a priori*.[9] It should be noted that the satellite retrieval procedure is intricate and the problem of 3D inhomogeneity in radiative transfer is one of many issues in developing a retrieval algorithm. The distribution of satellite data points on the constructed charts for a given satellite–Sun geometry can be converted to optical depth and DE using a minimization method. The 9 March case reveals that the cirrus pixels for this date consisted of a range of optical depths from 0 to 6. For optical depths smaller and larger than 1, the DE varies between 30 and 130 μm and between 70 and 130 μm, respectively.

A 3D cloud domain containing a 40 km × 300 km rectangular strip was chosen at which the center coincides with the ARM Central Facility site, while its orientation is along the wind direction. The vertical profiles of temperature and wind speed and direction from soundings launched at 2030, 2206, and 2329 UTC were used to determine the vertical IWC and ice crystal size using the cloud-level temperature sounding and following the cloud-top height determination developed by Hutchison *et al.*[30] In this case, the peak wind speed at the cloud level is approximately 40 m/s, and the wind direction is relatively constant and maintained at approximately 250°, approximately in the west–southwest direction. For illustration purposes, the 3D IWC and DE results are presented in *xy*, *yz*, and *xz* planes over a 120 km × 40 km × 9 km AVHRR data domain, as shown in Fig. 1 (left panel). The horizontal and vertical resolutions are of the order of 1 and 0.1 km, respectively. Substantial variability in IWC and DE is shown in the *xz* plane, as compared to those in the *yz* plane associated with the prevailing wind direction. Also noted is the increasing DE toward the cloud base. The black areas indicate that AVHRR data was not available.

The satellite-inferred 3D IWC and DE fields were compared to the ice crystal size distribution and IWC independently derived from the simultaneous *in situ* measurements by 2D optical probes on board the University of North Dakota Citation. The 2D probes measured ice crystal sizes in 25 μm increments (type C, from 25 to 100 μm) and in 100 μm increments (type P, from 25 to 2000 μm).[31] In this case, the aircraft descends from 9.5 to 6.5 km and the flight track between 2132 and 2223 UTC consists of a 12-loop Lagrangian spiral descending pattern centered at the ARM central facility site. Each loop took about 4 min to complete, and the aircraft descended 0.25 km per loop. Sampling of the ice crystal size was taken every 5 s. Following the method developed in Ou *et al.*,[22] we computed the *in situ* IWC and DE for each loop. Based on the soundings of local wind speed and direction, we also determined the latitude and longitude of the satellite's pixels that correspond to the location of each *in situ* sampling. For comparison purposes, we extracted the IWC and DE values from the 3D satellite-inferred cloud fields using the latitude and longitude of AVHRR pixels and the flight height and track. We then calculated the mean values for the pixels associated with each loop. The right panels in Fig. 1 illustrate comparison between collocated satellite-retrieved and *in situ* results. The re-
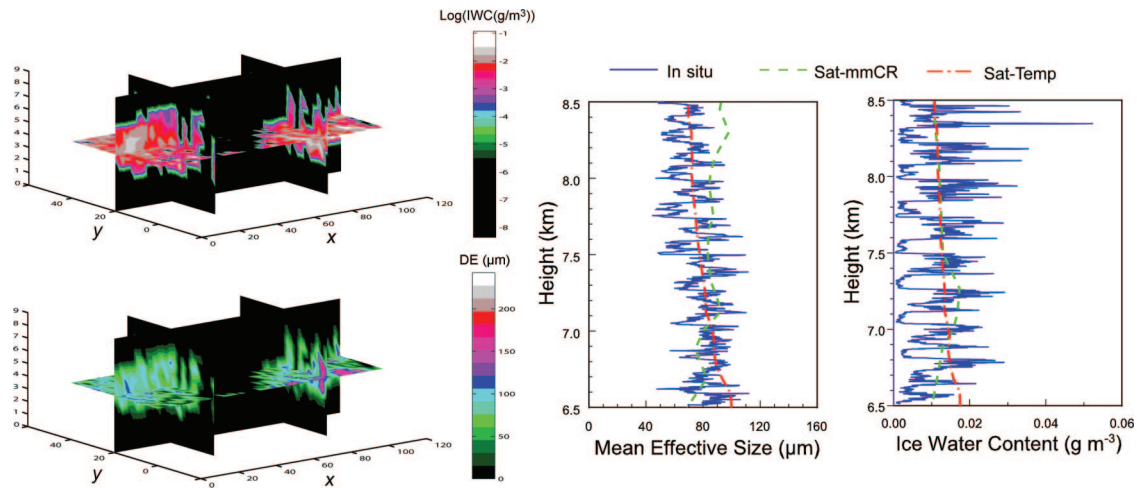
Fig. 1. (Color online) Left panel, 3D IWC, 0–0.1 g/m^3 and mean effective ice crystal size (DE, 0–200 μm) determined from a combination of the optical depth and DE retrieval from the 0.63 and 3.7 μm AVHRR channels aboard the NOAA-14 satellite and the IWC and DE determined from the temperature sounding over the ARM SGP CART site at 2023 UTC on 9 March 2000. The 3D IWC and DE results are presented in xy, yz, and xz planes over a 120 km $\times$ 40 km $\times$ 9 km domain. Right panels, comparison of the 3D DE and IWC values inferred from the satellite-temperature and satellite-mmCR approaches and *in situ* ice crystal measurements taken onboard the University of North Dakota Citation for the 9 March case.

trieved mean DEs varied between 70 and 90 μm, larger than those derived from *in situ* measurements at the height above 8 km, but generally within the range of observations below 8 km. Also, the computed mean IWC based on the measured ice crystal size distribution varies between 0.01 and 0.02 g/m^3 and is in general agreement with those derived from *in situ* measurements in terms of both magnitude and vertical pattern. Differences between the 3D horizontal means and *in situ* values result from the fact that the latter are instantaneous and localized measurements. For comparison purposes, Fig. 1 also shows the mean values of DE and IWC as functions of the aircraft height inferred from the satellite-mmCR approach.[3,19] The retrieved DE and IWC vary between 60 and 100 μm and between 0.01 and 0.02 g/m^3, respectively, also in the bulk range of those derived from *in situ* measurements and in line with the satellite-temperature retrieval results. However, the satellite-mmCR approach appears to be unable to produce the characteristics of increasing DE toward the cloud base.

On 18 April 1997, an area of single-layer cirrus cloud was hovering over the SGP Central Facility site at the NOAA-14 overpass. This case is particularly suitable for testing of the 3D cirrus mapping scheme developed above because the dimension of this cloudy area is about the size of a mesoscale model domain, and at the same time, there were collocated and coincident satellite and cloud microphysics data. The satellite-retrieved cloud optical depth and ice crystal mean effective size over a 0.4° $\times$ 2.0° domain around the Central Facility site reveal the area of relatively thick cirrus clouds extends from about 97.2° W to 98° W. A small area of thin cirrus exists around 96.5° W. The retrieved horizontal optical depth and DE range from 0 to 8 and from 0 to 150 μm, respec-

tively.[19] The sounding profiles over the Central Facility at about 2000 UTC show that the wind direction was from the west and the speed is relatively constant (~20 m/s) between 7 and 11 km. Using the cloud-level temperature sounding and through the parameterization described above, the vertical IWC and ice crystal mean size can be estimated. The 0.4° $\times$ 2.0° retrieval domain depicted in Fig. 2 is composed of 41 scan lines of AVHRR data in which each scan line contains 180 pixels. For the construction of 3D cloud fields, we narrowed the cloud field domain to 40 km and selected the AVHRR data from a box of 0.4° $\times$ 0.4°. The results are presented in xy, yz, and xz planes over a 40 km $\times$ 40 km $\times$ 4.5 km AVHRR data domain, as shown in Fig. 2. Substantial variability in IWC and DE is shown in the xz plane as compared to those in the yz plane associated with the prevailing wind direction (parallel to the y direction), and DE is shown to increase toward the cloud base.

The 3D IWC and DE fields for this case were compared to the ice crystal size distribution and IWC independently derived from the simultaneous *in situ* measurements by 2D probes onboard the University of North Dakota Citation. The flight track between 2018 and 2100 UTC consisted of a racetrack pattern in six ascending legs centered at the ARM central facility site near Lamont, Oklahoma. This period coincided with the NOAA-14 AVHRR overpass (~2023 UTC). The satellite and aircraft data extraction procedures are similar to those for the 9 March case. The right panels in Fig. 2 illustrate that the retrieved mean DEs varied between 60 and 120 μm, generally larger than those derived from *in situ* measurements by less than 10 μm. Also, the retrieved mean IWCs varied between 0 and 0.3 g/m^3, in general agreement with those derived from *in situ* measurements. In addition, it is noted that the DE and
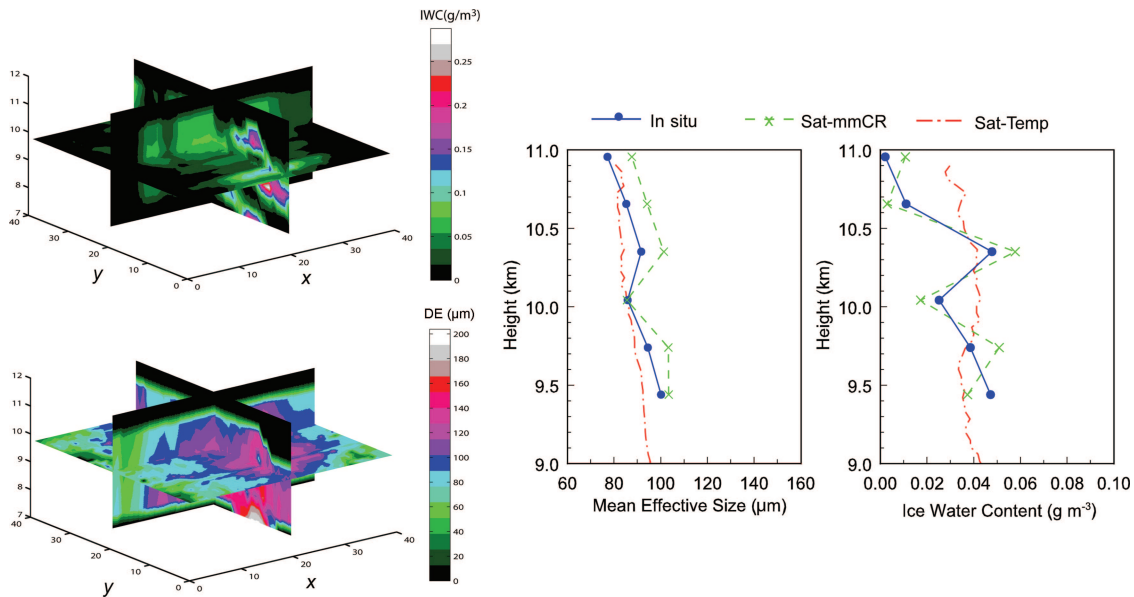
Fig. 2. (Color online) Left panel, 3D IWC (0–0.28 g/m³) and mean effective ice crystal size (DE, 0–196 μm) determined from a combination of the optical depth and DE retrieval from the 0.63 and 3.7 μm AVHRR–NOAA channels and the vertical IWC and DE inferred from a parameterization of temperature and cloud microphysics over the ARM SGP CART site at 2023 UTC on 18 April 1997. The 3D results are presented in xy, yz, and xz planes over a 40 km × 40 km × 4.5 km domain. Right panels, comparison of the averaged 3D IWC and DE values inferred from the satellite-temperature and satellite-mmCR approaches to those derived from *in situ* ice microphysics measurements from the University of North Dakota Citation as a function of aircraft leg height for the 18 April case.

IWC profiles from the satellite-mmCR approach agree well with those determined from the current method and *in situ* measurements.

In the preceding comparisons, differences between the 3D IWC and DE values inferred from satellite retrieval and *in situ* analysis could be attributed to a number of approximations made in the development of the remote sensing algorithm as well as the inherent uncertainty in geographical collocation and temporal coincidence between two data sources. The similarity between the retrieved and *in situ* derived IWC and DE values, however, is quite encouraging. Because of the limitation of the *in situ* measurement of small ice crystals[32] and the uncertainty of satellite retrieval of thin clouds,[33] we anticipate that the 3D cloud remote sensing technique developed herein is most applicable to cirrus clouds with optical depths greater than ~0.5 that contain ice crystals larger than ~20 μm.

3. Three-Dimensional Model for Laser Transmission-Backscattering through Inhomogeneous Clouds

A. Theoretical Basis

We consider 3D direct transmission and the transmission produced by multiple scattering along the laser beam. Figure 3(a) depicts a 3D laser-target geometry in which the aircraft is at the edge of and above an assumed rectangular slab of a cloud defined by a 3D dimension (x_c, y_c, z_c). The laser-target scan geometry is specified by a vertical scan angle, θ, which is the elevation angle of the laser beam, and a horizontal azimuthal angle, ϕ, which is the angle

between the flying direction of the aircraft and the projected direction of the laser beam on the xy plane. The positions of the airborne laser and the target are specified as (x_a, y_a, z_a) and (x_m, y_m, z_m), respectively. The coordinates of the incident (x_i, y_i, z_i) and exit (x_e, y_e, z_e) points of a laser beam at cloud boundaries can be determined from the laser-target scan geometry. The direct transmission through a 3D inhomogeneous cloudy atmosphere follows exponential attenuation and can be written in terms of the transmitted power F_d in the form

$$F_d = F_0 \exp\left[-\tau_c - \int_0^s \beta_e(s') \mathrm{d}s' \right], \qquad (3.1)$$

where

$$\tau_c = \beta_{\mathrm{nc},a} v + \beta_{\mathrm{nc},b} u, \qquad \beta_e = \beta_{\mathrm{air}} + \beta_{\mathrm{aer}} + k_v \rho + \beta_{\mathrm{cld}}.$$

In the above equations, F_0 is the laser power in watts; the total extinction coefficient β_e is the sum of the scattering coefficient of air molecules β_{air}, the extinction coefficient of aerosols β_{aer}, the absorption coefficient of water vapor times water vapor density $k_v \rho$, and the extinction coefficient of cloud particles β_{cld} along the path of the laser beam; and the exponential attenuation outside the cloud is also accounted for in Eq. (3.1), where $\beta_{\mathrm{nc},a}$ and $\beta_{\mathrm{nc},b}$ are extinction coefficients due to noncloud species (air molecules, aerosols, and water vapor) above and below the cloud, respectively. The parameter u denotes the distance BTg between the cloud base and the target and v
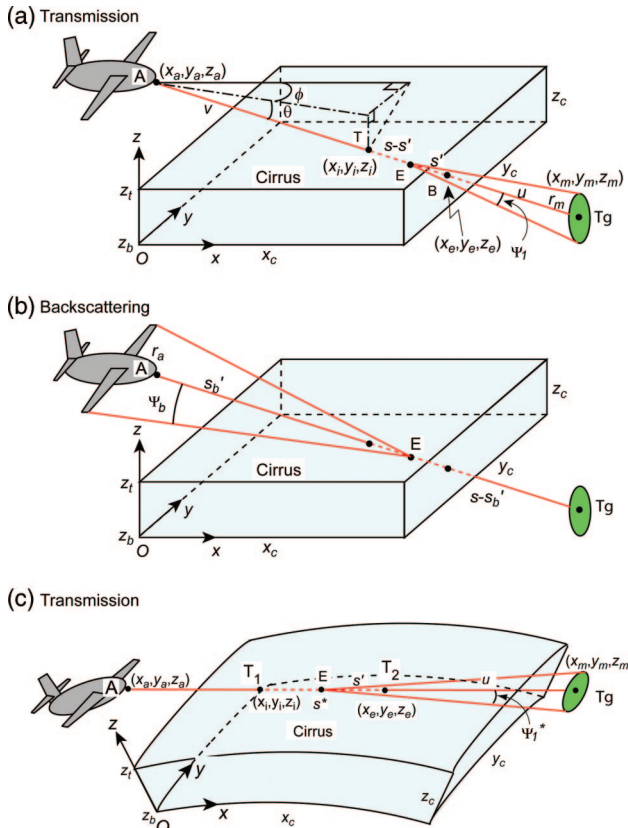
(a) Transmission

(b) Backscattering

(c) Transmission

Fig. 3. (Color online) (a) Laser transmission through a 3D cloud. The positions (x_a, y_a, z_a), (x_m, y_m, z_m), (x_i, y_i, z_i), and (x_e, y_e, z_e) denote coordinates of the airborne laser, target, incident point, and exit point; (x_c, y_c, z_c) is the 3D cloud dimension, where $z_c = z_t - z_b$; θ is a laser scan angle; ϕ is a horizontal azimuthal angle; Ψ_1 is an angle subtended by the target at point E; r_m is the effective radius of the target; $s' = EB$; $u = BTg$; $v = AT$; and $s - s' = ET$. (b) Laser backscattering through a 3D cloud. Ψ_b is the angle subtended by the aircraft at point E, r_a is the effective radius of the aircraft, $s - s_b' = ETg$, and $s_b' = EA$. (c) Laser transmission through a 3D inhomogeneous cloud in a spherical atmosphere. All symbols are the same as in (a), except that $s^* = T_1T_2$, $s' = ET_2$, $u = T_2Tg$, and Ψ_1^* is an angle subtended by the target at point E.

denotes the distance AT between the aircraft and the cloud top. In the present study, β_{aer} is obtained from the MODTRAN default profile, and ρ is taken from the U.S. Standard Atmosphere.

In reference to Fig. 3(a), the parameter s' is the distance along the laser beam between a point (x, y, z) in the cloud and the exit point at the cloud boundary defined by

$$s' = (z - z_b)/\mu, \qquad (3.2)$$

where μ is $\sin|\theta|$, z_b is the cloud-base height, and θ is the scan angle of the laser beam in the xz plane given by

$$\theta = \tan^{-1}[\cos \phi(z_m - z_a)/(x_m - x_a)], \qquad (3.3)$$

with ϕ being the azimuthal angle of the laser beam:

$$\phi = \tan^{-1}[(y_m - y_a)/(x_m - x_a)]. \qquad (3.4)$$

The distance along the laser beam between the cloud top and base is given by

$$s = (z_t - z_b)/\mu = \{(x_e - x_i)^2 + (y_e - y_i)^2 + (z_e - z_i)^2\}^{1/2}, \qquad (3.5)$$

where z_t is the height of the cloud top. The points (x_a, y_a, z_a), (x_m, y_m, z_m), (x_i, y_i, z_i), and (x_e, y_e, z_e) are the coordinates of the aircraft, the target, and the incident and emergent points of the laser beam on the cloud, respectively. The parameters x_c, y_c, and z_c denote the 3D cloud dimensions.

Formulation of the first-order scattering in the 3D case is similar to the 2D case and can be written in the form

$$F^{(1)}(0, \Omega) = \exp(-\tau_c) \int_0^s J^{(1)}(s', \Omega)$$

$$\times \exp\left[-\int_0^{s'} \beta_e(s'')ds''\right]\beta_e(s')ds'. \qquad (3.6)$$

However, the path lengths s' and s are functions of 3D cloud geometry defined in Eqs. (3.2)–(3.5). Based on the successive-order-of-scattering approach, the first-order source function for forward scattering is given by

$$J^{(1)}(s', \Omega) = \frac{\varpi(s')}{2} F^{(0)}(s', \Omega) \int_0^{\Psi_1} P_{cld}(\Theta, s')\sin \Theta d\Theta, \qquad (3.7a)$$

where the term

$$F^{(0)}(s', \Omega) = F_0 \exp\left[-\int_{s'}^s \beta_e(s'')ds''\right]. \qquad (3.7b)$$

The single-scattering albedo, $\varpi(s')$, and the phase function of cloud particles, P_{cld}, are functions of s' involving 3D geometry, and the angle Ψ_1 within which scattering occurs is given by $\tan^{-1}[r_m/(u + s')]$. Note that the phase function for aerosols (and air molecules) in forward directions is more than two orders smaller than that for ice particles, and for practical purposes the former can be neglected in forward-scattering calculations.

In a manner similar to the first-order forward-scattering formulation, the source function that is due to the first-order backscattering can be expressed in the form

$$J^{(1)}(s_b', \Omega) = \frac{\varpi(s_b')}{2} F^{(0)}(s_b', \Omega) \int_{\pi - \Psi_b}^{\pi} P_{ave}(\Theta, s_b')$$

$$\times \sin \Theta d\Theta, \qquad (3.8a)$$

where the term

$$F^{(0)}(s_b', \, \Omega) = F_0 \exp\left[-\int_0^{s_b'} \beta_e(s'')\mathrm{d}s'' \right]; \quad (3.8b)$$

s_b' is the distance from the aircraft to a point along the laser beam, as shown in Fig. 3(b); and $P_{\mathrm{ave}}(\Theta, s_b')$ is the phase function that accounts for both cloud and aerosol particles. For backscattering, contribution from aerosols becomes significant when thin cirrus clouds are involved, and the angle Ψ_b is given by $\tan^{-1}(r_a/s_b')$, where r_a denotes the effective radius of the aircraft. Note that the phase functions for aerosols and air molecules are of the same order as that for cloud particles and must be accounted for in the analysis. Thus formulations for the first-order forward [Eqs. (3.6), (3.7a), and (3.7b)] and backward scattering [Eqs. (3.8a) and (3.8b)] differ not only in geometry but also in the use of the phase function.

Furthermore, using the principle of successive order of scattering along the laser beam, the nth-order scattering can be expressed by

$$F^{(n)}(0, \, \Omega) = \exp(-\tau_c)\int_0^{s} J^{(n)}(s', \, \Omega)$$
$$\times \exp\left[-\int_0^{s'} \beta_e(s'')\mathrm{d}s'' \right]\beta_e(s')\mathrm{d}s', \quad (3.9)$$

where the source function

$$J^{(n)}(s', \, \Omega) = \frac{\varpi(s')}{2}\int_{\Theta_n-\Psi_n}^{\Theta_n+\Psi_n} F^{(n-1)}(s', \, \Omega)P_{\mathrm{cld}}(\Theta, \, s')$$
$$\times \sin \Theta \mathrm{d}\Theta, \quad (3.10)$$

where Θ_n denotes the scattering angle within which the nth-order scattering contributes to the source function integral, and Ψ_n is an angle associated with Θ_n determined by the scattering geometry. Likewise, the nth-order backscattering can also be expressed in a similar form.

The distance between the aircraft and the engaging target is generally of the order of hundreds of kilometers. To accurately simulate laser transmission along such a long path length, the sphericity of the cloud-top surface due to the Earth's curvature must be taken into account. As illustrated in Fig. 3(c), we consider the geometry where both the aircraft and the target are above the cloud. The direct transmission of a laser beam in a 3D spherical geometry, F_d^*, is similar to Eq. (3.1) and can be expressed by

$$F_d^* = F_d F_s, \quad (3.11)$$

where F_d is the direct transmission for the clear-sky line of sight, and F_s is an additional cloud transmission produced by spherical geometry. When both the air-

craft and target are above the cloud, F_s is defined by

$$F_s = \exp\left[-\int_0^{s^*} \beta_e(s')\mathrm{d}s' \right], \quad (3.12)$$

where s^* is the distance along the laser beam between the incident (x_i, y_i, z_i) and exit (x_e, y_e, z_e) points at the cloud top, and s' is the distance along the laser beam between a point in the cloud and the exit (x_e, y_e, z_e) point at the cloud top. Forward scattering is the sum of the forward scattering produced in the plane-parallel geometry, $F^{(1)}(0, \Omega)$, plus the forward scattering in the portion of the cloudy atmosphere that is related to the spherical geometry:

$$F^{*(1)}(0, \, \Omega) = F^{(1)}(0, \, \Omega) + F_s{}^{(1)}(0, \, \Omega). \quad (3.13)$$

On the basis of the successive order-of-scattering approach, the second term is given by

$$F_s{}^{(1)}(0, \, \Omega) = \exp(-\tau_c)\int_0^{s^*} J^{(1)}(s', \, \Omega)$$
$$\times \exp\left[-\int_0^{s'} \beta_e(s'')\mathrm{d}s'' \right]\beta_e(s')\mathrm{d}s', \quad (3.14)$$

where s^* is the distance between the incident and exit points. The expression for the source function $J^{(1)}(s', \Omega)$ in Eq. (3.14) is the same as that defined in Eqs. (3.7a) and (3.7b), except that the angular integration limits are determined by a new angle Ψ_1^* and the path-length integration for the direct transmission is from 0 to $(s^* - s')$. Likewise, the source function due to the first-order backscattering can be obtained from the angular and path-length integration. Furthermore, the nth-order scattering terms for transmission and backscattering are the same as those defined in Eqs. (3.9) and (3.10), except for the angular and path-length integration limits that follow the spherical geometry formulation.

B. Application of the Satellite-Inferred Three-Dimensional Results to Three-Dimensional Laser Transmission and Backscattering

We investigate the sensitivity of laser transmission and backscattering on variation in the cloud optical depth, particle size, and cloud-base height, as well as the positions of the aircraft and target. In particular, we study deviation of the 2D transmission and backscattering results from the present 3D values using the same cloud properties. Here 2D implies that a cloud field is averaged over the y direction for laser transmission and backscattering formulations.[18]

Figure 4 shows three vertical transects at $y = 1$, 20, and 39 km corresponding to the 3D cirrus cloud IWC and DE determined for the 18 April 1997 case discussed above. The aircraft (laser beam) is shown at
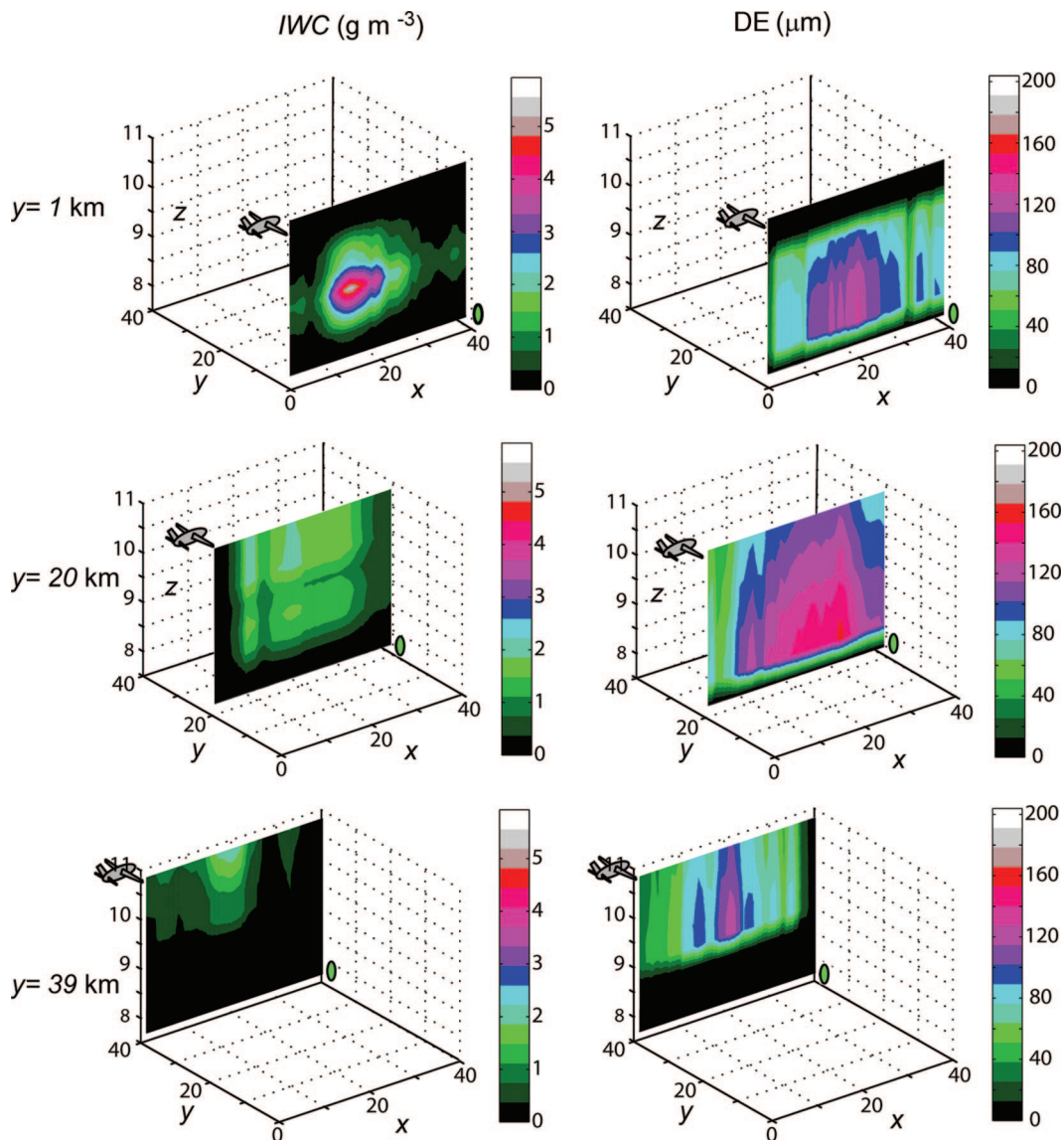
Fig. 4. (Color online) 3D cirrus IWC and DE fields mapped at $y = 1$, 20, and 39 km obtained for the 18 April 1997 case over the ARM SGP Central Facility. The dark areas are areas with no observations. Also shown are the positions of the aircraft and the moving target.

the left upper edge ($x = 0$, $z = z_a$) of these diagrams, while the target is located at the right edge ($x = x_m$). These transects of cirrus cloud properties differ significantly and therefore cannot be assumed to be homogeneous in the y direction. For example, the IWC transect at $y = 1$ km shows an area of maximum values near $x = 15$ km and $z = 9$ km, whereas at $y = 20$ and 39 km, there is no such maximum. Moreover, the D_e transect shows a maximum at $y = 20$ km.

In Fig. 5, we present the mean and standard deviation of 3D results for direct transmission and first-order forward and backward scattering based on the five vertical transects (1, 11, 20, 29, and 39 km) as functions of target height. The standard deviation is denoted by a horizontal bar. For comparison purposes, the 2D results are also displayed (dotted curves). Substantial differences are shown between 2D and the 3D mean, particularly in the cloud region

for larger optical depth. For direct transmission and first-order scattering, standard deviations are larger inside the cloud since the path length within the cloud is longer and the laser transmission is strongly subject to cloud inhomogeneity. For first-order backscattering, standard deviations in the cloud are smaller, since it is primarily determined by the cloud-top portion near the aircraft. The total transmission, the sum of direct transmission and first-order scattering, may be expressed in a parameterized form, $\exp(-\tau^*/\mu)$, where $\tau^*(\sim 0.95–0.99)$ is an adjusted optical depth accounting for both contributions. Backscattering depends on the characteristics of the particles' phase function and the intricate geometry involving laser and target. For this reason, development of an analytical model for physical explanation is not straightforward.

Finally, the effects of the Earth's sphericity on laser transmission and backscattering were evaluated. Fig-
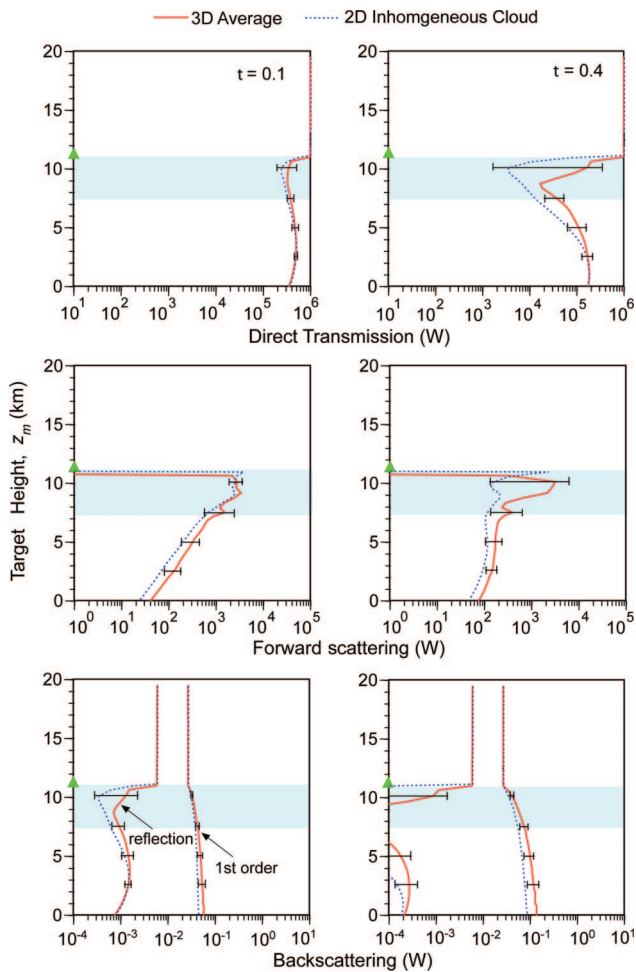
Fig. 5. (Color online) Direct transmission, forward scattering, and backscattering for a 2D inhomogeneous (averaged over the y direction) and mean values of those for the 3D cirrus cloud field based on the five vertical transects (1, 11, 20, 29, and 39 km) are displayed. Standard deviations of the 3D mean values based on the five 3D transect values are also plotted in terms of horizontal bars. $\lambda = 1.315\ \mu\text{m}$, $F_0 = 10^6\ \text{W}$, $R_\lambda = 0.2$, $r_a = 4\ \text{m}$, $z_a = 11.2\ \text{km}$, $z_t = 11.1\ \text{km}$, and $z_b = 7.5\ \text{km}$.
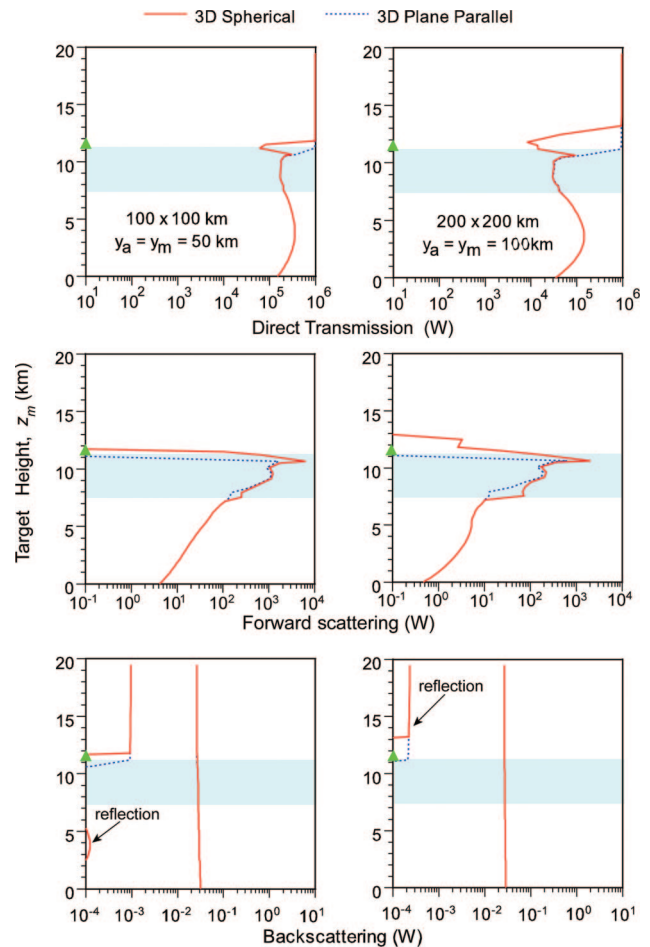

Fig. 6. (Color online) Comparisons of the direct laser transmission, forward-scattering transmission, and backscattering for cloud fields in plane-parallel and spherical atmospheres assuming horizontal distances of 100 and 200 km. The 3D cloud fields (40 km × 40 km in the horizontal) are adjusted to fit in the 100 km × 100 km and 200 km × 200 km dimensions.

ure 6 shows plots for the 3D direct transmission and first-order forward scattering and backscattering through 100 km × 100 km × 4.5 km and 200 km × 200 km × 4.5 km cloud fields embedded in spherical and plane-parallel atmospheres. The 3D cloud horizontal fields of 40 km × 40 km are adjusted uniformly to fit in the 100 km × 100 km and 200 km × 200 km dimensions for the purpose of understanding the effect of the Earth's curvature on laser transmission. For direct transmission, the effect of a spherical Earth is more significant for a longer horizontal distance of 200 km than 100 km, particularly when the target height is between the cloud top and 2 km above it, where transmission can be significantly reduced (by two orders of magnitude) by the Earth's curvature. The forward scattering is enhanced near the cloud top due to the additional scattering by laser transmission through the curved cloud-top portion. The slight fluctuation above the cloud is due to localized strong scattering near the cloud top. The effects of the spherical geometry on the first-order backscattering and reflection from the target are small because of small backscattering values. For both Figs. 5 and 6, the results do not show sensitivity to cloud inhomogeneity above $z = 12$ km. However, we have included the curves above this height to be consistent with the format in our previous papers published in this journal.[17,18]

4. Concluding Remarks

We have developed an approach for the determination of 3D IWC and DE fields of cirrus clouds based on a combination of satellite-retrieved optical depth and DE in a horizontal plane and the vertical IWC and DE determined through a parameterization of cloud microphysics and temperature. To investigate the reliability of this parameterization approach for the mapping of 3D cloud fields, we have selected AVHRR–NOAA data associated with the single-layer cirrus clouds that occurred at the ARM SGP CART site in the northern Oklahoma area on 18 April 1997 and 9

March 2000 during a Spring Cloud IOP. Retrieval and analysis were carried out to construct 3D IWC and DE fields from the AVHRR data, which were then compared to collocated and coincident *in situ* measurements of the ice crystal size distribution and IWC independently derived from the optical probes onboard the University of North Dakota Citation. The satellite-retrieved 3D IWC and DE values show a general and consistent agreement with the concurrent and collocated airborne microphysics measurements. The accuracy of small ice crystals in both *in situ* measurements and satellite remote sensing is a subject requiring further investigation.

A 3D laser transmission and backscattering model for inhomogeneous clouds, particularly applicable to high thin cirrus, has been developed for an aircraft-target system. We approached this problem by using the principle of the successive order of scattering for radiative transfer in which the attenuation and scattering of a laser beam can be traced in accordance with the scattering geometry for clouds in plane-parallel and spherical atmospheres. For transmission, the direct component, the first-order scattering, and the nth-order multiple scattering were formulated by means of the source-function technique in the context of the successive-order-of-scattering approach. Similar formulations were carried out for backscattering involving the laser energy available at the position of the aircraft. We performed numerical simulation of the transmitted and backscattered laser energies for a 3D inhomogeneous cirrus cloud field. The simulation results for 3D direct transmission, forward-scattered transmission, and backscattering have been compared to those for the 2D model and substantial differences are shown. The effect of the Earth's curvature becomes particularly important for long path transmission involving the airborne laser and moving target engagement.

In the present study, we have used the AVHRR–NOAA data for the construction of 3D cloud fields in view of the availability of collocated and coincident airborne ice microphysics measurements for validation purposes. However, the parameterization approach developed in this paper can be directly applied to the data sets from MODIS onboard the NASA Terra and Aqua satellites as well as the future visible–infrared imager radiometer suite channels to be included in the National Polar-orbiting Operational Environmental Satellite System platform for the 3D cirrus cloud study. The availability of these satellite data for 3D cloud mapping can be directly employed in connection with the simulation of 3D airborne laser transmission and backscattering in spherical atmospheres for tactical application.

References

1. K. Sassen, "The polarization lidar technique for cloud research: a review and current assessment," Bull. Am. Meteorol. Soc. **72,** 1848–1866 (1991).

2. J. D. Spinhirne and W. D. Hart, "Cirrus structure and radiative parameters from airborne lidar and spectral radiometer observations: the 28 October 1986 FIRE study," Mon. Weather Rev. **118,** 2329–2343 (1990).

3. G. G. Mace, A. J. Heymsfield, and M. R. Poellot, "On retrieving the microphysical properties of cirrus clouds using the moments of the millimeter-wavelength Doppler-spectrum," J. Geophys. Res. **107,** doi:10.1029/2001JD001308 (2002).

4. L. M. Miloshevich and A. J. Heymsfield, "A balloon-borne continuous cloud particle replicator for measuring vertical profiles of cloud microphysical properties: instrument design, performance, and collection efficiency analysis," J. Atmos. Ocean. Technol. **14,** 753–768 (1997).

5. Y. Gu and K. N. Liou, "Radiation parameterization for three-dimensional inhomogeneous cirrus clouds: application to climate models," J. Clim. **14,** 2443–2457 (2001).

6. K. N. Liou, "Cirrus clouds and Climate, in *McGraw-Hill 2005 Yearbook of Science & Technology* (McGraw-Hill, 2005), pp. 51–53.

7. P. Rolland, K. N. Liou, M. D. King, S. C. Tsay, and G. M. McFarquhar, "Remote sensing of optical and microphysical properties of cirrus clouds using MODIS channels: methodology and sensitivity to assumptions," J. Geophys. Res. **105,** 11,721–11,738 (2000).

8. S. C. Ou, K. N. Liou, Y. Takano, G. J. Higgins, A. George, and R. Slonaker, "Remote sensing of cirrus cloud optical thickness and effective particle size for the National Polar-Orbiting Operational Environmental Satellite System Visible/Infrared Imager Radiometer Suite: sensitivity to instrument noise and uncertainties in environmental parameters," Appl. Opt. **42,** 7202–7214 (2003).

9. S. C. Ou, K. N. Liou, M. D. King, and S. C. Tsay, "Remote sensing of cirrus clouds parameters based on a 0.63–3.7 μm radiance correlation technique applied to AVHRR data," Geophys. Res. Lett. **26,** 2437–2440 (1999).

10. M. D. King, S. Platnick, P. Yang, G. T. Arnold, M. A. Gray, J. C. Riedi, S. A. Ackerman, and K. N. Liou, "Remote sensing of liquid water and ice cloud optical thickness and effective radius in the arctic: application of airborne multispectral MAS data," J. Atmos. Ocean. Technol. **21,** 857–875 (2004).

11. P. Minnis, K. N. Liou, and Y. Takano, "Inference of cirrus cloud properties using satellite observed visible and infrared radiance. Part I: Parameterization of radiance field," J. Atmos. Sci. **50,** 1279–1304 (1993).

12. B. A. Baum, T. Uttal, M. Poellot, T. P. Ackerman, J. M. Alvarez, J. Intrieri, D. O'C. Starr, J. Titlow, V. Tovinkere, and E. Clothiaux, "Satellite remote sensing of multiple cloud layers," J. Atmos. Sci. **52,** 4210–4230 (1995).

13. D. Wylie, D. Jackson, P. Menzel, and J. Bates, "Trends in global cloud cover in two decades of HIRS observations," J. Clim. **18,** 3021–3031 (2005).

14. J. Roskovensky and K. N. Liou, "Detection of thin cirrus using a combination of 1.38 μm reflectance and window brightness temperature difference," J. Geophys. Res. **108,** doi:10.1029/2002JD003346 (2003).

15. J. K. Roskovensky and K. N. Liou, "Differentiating airborne dust from cirrus clouds using MODIS data," Geophys. Res. Lett. **32,** doi:10.1029/2005GL022798 (2005).

16. K. N. Liou, Y. Takano, S. C. Ou, A. Heymsfield, and W. Kreiss, "Infrared transmission through cirrus clouds: a radiative model for target detection," Appl. Opt. **29,** 1886–1896 (1990).

17. K. N. Liou, Y. Takano, S. C. Ou, and M. W. Johnson, "Laser transmission through thin cirrus clouds," Appl. Opt. **39,** 4886–4894 (2000).

18. S. C. Ou, Y. Takano, K. N. Liou, R. J. Lefevre, and M. W. Johnson, "Laser transmission-backscattering through inhomogeneous cirrus clouds," Appl. Opt. **41,** 5744–5754 (2002).

19. K. N. Liou, S. C. Ou, Y. Takano, J. Roskovensky, G. Mace, K. Sassen, and M. Poellot, "Remote sensing of three-dimensional inhomogeneous cirrus clouds using satellite and mm-wave cloud radar data," Geophys. Res. Lett. **29,** doi:10.1029/2002GL014846 (2002).

20. K. F. Evans and W. J. Wiscombe, "An algorithm for generating stochastic cloud fields from radar profile statistics," Atmos. Res. **72,** 263–289 (2004).

21. R. J. Hogan and S. F. Kew, "A 3D stochastic cloud model for investigating the radiative properties of inhomogeneous cirrus clouds," Q. J. R. Meteorol. Soc. **131,** 2585–2608 (2005).

22. S. C. Ou, K. N. Liou, Y. Takano, N. X. Rao, Q. Fu, A. J. Heymsfield, L. M. Miloshevich, B. Baum, and S. A. Kinne, "Remote sounding of cirrus cloud optical depths and ice crystal sizes from AVHRR data: verification using FIRE-II-IFO composite measurements," J. Atmos. Sci. **52,** 4143–4158 (1995).

23. A. J. Heymsfield and C. M. R. Platt, "A parameterization of the particle size spectrum of ice clouds in terms of the ambient temperature and ice water content," J. Atmos. Sci. **41,** 846–855 (1984).

24. S. C. Ou and K. N. Liou, "Ice microphysics and climatic temperature feedback," Atmos. Res. **35,** 127–138 (1995).

25. K. N. Liou, *Radiation and Cloud Processes in the Atmosphere: Theory, Observation, and Modelling* (Oxford U. Press, 1992), 487 pp.

26. G. M. McFarquhar and A. J. Heymsfield, "The definition and significance of an effective radius for ice clouds," J. Atmos. Sci. **55,** 2039–2052 (1998).

27. M. D. Goldberg, Y. Qu, L. M. McMillin, W. Wolf, L. Zhou, and M. Divakarla, "AIRS near-real-time products and algorithms in support of numerical weather prediction," IEEE Trans. Geosci. Remote Sens. **41,** 379–389 (2003).

28. R. Kistler, E. Kalnay, W. Collins, S. Saha, G. White, J. Woollen, M. Chelliah, W. Ebisuzaki, M. Kanamitsu, V. Kousky, H. van den Dool, R. Jenne, and M. Fiorino, "The NCEP-NCAR 50-year reanalysis: monthly means CD-ROM and documentation," Bull. Am. Meteorol. Soc. **82,** 247–268 (2001).

29. Q. Fu and K. N. Liou, "Parameterization of the radiative properties of cirrus clouds," J. Atmos. Sci. **50,** 2008–2025 (1993).

30. K. D. Hutchison, E. Wong, and S. C. Ou, "Cloud base height retrieval during nighttime conditions with MODIS data," Int. J. Remote Sens. **27,** 2847–2862 (2006).

31. A. J. Heymsfield and D. Baumgardner, "Summary of a workshop on processing 2-D probe data," Bull. Am. Meteorol. Soc. **66,** 437–440 (1985).

32. A. Kristensson, J.-F. Gayet, J. Ström, and F. Auriol, "*In situ* observations of a reduction in effective crystal diameter in cirrus clouds near flight corridors," Geophys. Res. Lett. **27,** 681–684, 10.1029/1999GL010934 (2000).

33. P. Rolland and K. N. Liou, "Surface variability effects on the remote sensing of thin cirrus optical and microphysical properties," J. Geophys. Res. **106,** 22,965–22,977 (2001).